Journal of the European Ceramic Society 45 (2025) 117144

Contents lists available at ScienceDirect

Journal of the European Ceramic Society

journal homepage: www.elsevier.com/locate/jeurceramsoc

Rapid debinding and sintering of alumina ceramics fabricated by direct ink writing

Subhadip Bhandari [a], Ondrej Hanzel [b], Milad Kermani [c], Vincenzo M. Sglavo [c], Mattia Biesuz [c,*], Giorgia Franchin [a,*]

[a] Department of Industrial Engineering, University of Padova, Via Marzolo 9, Padova 35131, Italy
[b] Institute of Inorganic Chemistry, Slovak Academy of Sciences, Dúbravska cesta 9, Bratislava 84536, Slovakia
[c] Department of Industrial Engineering, University of Trento, Via Sommarive 9, Trento 38122, Italy

ARTICLE INFO

Keywords:
Ultrafast high-temperature sintering
Pressureless spark plasma sintering
Fast firing
Debinding
Al_2O_3
Direct ink writing
Additive manufacturing

ABSTRACT

Direct ink writing (DIW) is a widely used additive manufacturing technique to fabricate complex-shaped ceramics. Unlike vat photopolymerization or fused filament fabrication, the limited amount of binder in DIW facilitates rapid debinding. In this study, alumina inks with suitable rheology were prepared with two different ceramic loadings (42.8 vol% and 48.1 vol%). Subsequently, log-pile structures were printed using two different nozzle diameters (0.41 mm and 0.84 mm). The fabricated samples were dried at room temperature and subjected to different rapid sintering procedures: ultra-fast high temperature sintering (UHS), pressureless spark plasma sintering (PSPS) and fast-firing (FF). Both UHS and PSPS successfully densified the samples in Ar without any defects. Conversely, the fast-firing in air resulted in some cracks, with the intensity of failures increasing with the nozzle size. UHS and PSPS allowed for nearly fully dense materials with refined microstructure which are not achievable by conventional heating.

1. Introduction

Over the recent years, additive manufacturing (AM) has seen significant growth and development. Unlike metals, which are more amenable to be shaped by plastic deformation and subtractive manufacturing methods, ceramics are inherently brittle and this makes the production of complex shapes using traditional techniques difficult; from this point of view additive manufacturing appears as a suitable technology for fabricating intricate ceramic components.

According to ASTM, AM technologies can be categorized into seven different forms [1]; among them material-extrusion-based methods, and especially direct ink writing (DIW), are of particular interest to fabricate various ceramic compositions [2,3]. DIW is faster and cheaper than other AM methods because the printing tools are open source and it is possible to produce different materials like ceramics, plastics, metals and composites [4]. Moreover, one can prepare a very small amount of ink with the micro-extrusion process, thereby minimizing the waste of material [2].

Ink rheology plays a crucial role in determining the success or failure of the printed components [5]. The addition of different additivities (binder, plasticizer and dispersant) to the solvent / ceramic powder mix ensures that the formulated ink has a suitable visco-elastic response, exhibiting shear-thinning behaviour during the extrusion and shape retention thereafter. Usually, water is used as solvent for formulating highly loaded inks, and it dries up quickly when the printed samples are kept at room temperature [2]. Such rapid drying can induce defects in the sample in form of warping or cracks. To mitigate these issues, drying can be carried out in controlled humidity environment [6] and alternative solvents (like glycerol) can be used [7].

In DIW, a key advantage is that the solvent (which is usually water) evaporates easily from the sample. This leaves behind only a very limited amount of organic additives that needs to thermally debinded during the heat treatment process [8]. In contrast to other AM techniques such as vat photopolymerization or fused filament fabrication, where the binder does not evaporate, debinding the samples can be more challenging.

The debinding and sintering of printed components represent the most time-consuming and energy-intensive step of the manufacturing process. In recent years, there has been significant research towards rapid sintering techniques either to enhance the properties or to reduce

* Corresponding authors.
E-mail addresses: Mattia.biesuz@unitn.it (M. Biesuz), giorgia.franchin@unipd.it (G. Franchin).

https://doi.org/10.1016/j.jeurceramsoc.2024.117144
Received 5 October 2024; Received in revised form 3 December 2024; Accepted 6 December 2024
Available online 9 December 2024

the environmental and economic costs of firing [9,10]. Among these, those which appear very promising for AM are pressureless-spark plasma sintering (PSPS) [11], ultrafast high-temperature sintering (UHS) [12], and fast firing (FF) [11].

FF is a rapid sintering technique where the furnace is preheated to a desired temperature and then the sample is introduced in it for a short time [13]. As a result, the sample experiences a heating rate in the order of 10^2 – 10^3 °C/min, which results in enhanced densification and fine microstructure [14–17].

PSPS is a slightly modified form of SPS where the graphite die is designed such that there no pressure is applied to the sample [18]. The current passing through the die heats it up (with 50 – 1000 °C/min) and this heat is transferred to the sample within the die mostly by radiation.

UHS is the latest technique developed in the field of ceramic sintering. The green body is sandwiched between a graphite felt, which is connected to a power supply. As soon as this is turned on, heat is generated in the felt by the Joule effect and transferred to the sample [11,12,19–31]. Consequently, this experiences a heating and cooling at approximately 10^3 – 10^5 °C/min, leading to enhanced densification in a few seconds [9]. Due to the use of graphite as a heating element (die or felt), PSPS and UHS are carried out in inert atmosphere to prevent oxidation, while FF is carried out in air.

In recent years, several studies have reported the use of PSPS to sinter additively manufactured components [32–35]. However, with the exception of one study [35], the debinding of the printed material was carried out before subjecting it to rapid heating in PSPS. More recently, also UHS has been used for debinding and sintering log-pile structures made of $BaTiO_3$ as a model ceramic system [11] but the density was limited (≈ 72 %) as a result of the h-$BaTiO_3$ formation in inert atmosphere. As such, so far, no DIW ceramic structure has been consolidated to high density *via* UHS. Moreover, in our previous study using ceramic filaments [12], the process was technologically different compared to the current work with DIW. The filament-based method required a chemical debinding step prior to the rapid heat treatment process. Additionally, the samples were fabricated using a nozzle with a diameter of 0.41 mm and were successfully sintered to densities exceeding 99 % under optimized processing conditions. In contrast, the current work with DIW eliminates the need for chemical debinding, relying instead on a simpler process that integrates shaping, drying, and sintering. Furthermore, the impact of varying the nozzle diameter and the sintering atmosphere on the rapid debinding and sintering process was not explored, which could potentially influence the whole process.

Although the limited organic content in the DIW ink makes rapid debinding less challenging compared to techniques like FFF or VP (Vat photopolymerization) and some reports on PSPS of DIW structures already exist, still an open question remains: Is it possible to debind and sinter structure obtained by DIW in a matter of 1–2 minutes? In other words, is it possible to go beyond the heating rates commonly achievable by PSPS? The goal of the present work was to use UHS for the very rapid debinding and sintering of DIW-produced alumina lattices to near full density. Alumina (Al_2O_3) was particularly chosen, as it is well-suited for sintering in inert conditions, with numerous reports demonstrating its ability to achieve very high density under such conditions [23,45]. Additionally, it is one of the most commonly used ceramic model systems for proof-of-concept studies. The effect of different printing parameters (i.e., the ceramic loading and nozzle diameter) on the rapid consolidation of the material was analysed and the results were compared to those obtained by using alternative rapid sintering techniques like PSPS and FF.

2. Materials and methods

The ink for the DIW process was formulated using Al_2O_3 powder (CT LS 3000SG, Almatis, SSA=7.80 m^2/g, d_{50} = 0.5 µm and d_{90} = 2 µm), Na-polyacrylic acid (Aldrich Chemistry) as dispersant, Na-alginate (Panreac AppliChem) as binder, glycerol (Prolabo) as humectant and distilled water as solvent. The alumina powder was manually sieved (100 µm mesh) to break the agglomerates, which otherwise might lead to nozzle clogging. Inks with two different ceramic loadings were prepared and the composition is reported in Table 1. The ink with higher organic content is labelled as HB, while the other with lower organic content is labelled as LB.

Table 1
Ink composition of the formulated inks in this study.

Ingredients (wt%)	High organic content (HB)	Low organic content (LB)
Al_2O_3	74	78
Binder + Dispersant + humectant	5.5	4.5
Solvent	20.5	17.5

Table 2
Summary of all sintering methods and parameters used in this study (UHS power refers here to the power peak).

Labelling	Sintering conditions	Labelling	Sintering conditions
UHS1	78 W; 60 s	PSPS1	1500 °C; 30 min
UHS2	168 W; 60 s	PSPS2	1500 °C; 60 min
UHS3	220 W; 60 s	PSPS3	1600 °C; 30 min
UHS4	265 W; 60 s	PSPS4	1600 °C; 60 min
UHS5	310 W; 60 s	FF	Preheated furnace at 1400 – 1550 °C (steps of 50 °C); 5 min
UHS6	301 W; 90 s	CS	1400 – 1600 °C (steps of 50 °C); 60 min
UHS7	309 W; 180 s		

Initially, the dispersant and the humectant were added to deionized water to prepare a homogenous solution. Thereafter, binder and powder were mixed and added stepwise to the solution. Following each addition, the ink was homogenously mixed using a planetary mixer (ARE-250, THINKY) for 2 min at 2000 rpm. A special water-cooled container was used during the mixing process to minimize water evaporation. The prepared ink was then transferred to a 30 ml syringe and then defoamed with the same planetary mixer at 2200 rpm for 3 min to remove possible entrapped air bubbles.

The defoamed syringe was then connected to a digital pressure-controlled fluid dispenser DC 300 (Vieweg GmbH) and mounted on the Delta Wasp 2040 Turbo 2 (WASP) to print log-pile structures (10 × 10 × 3 mm^3) with two different conical nozzle diameters (0.41 mm and 0.84 mm). The infill density was set to 50 % for both cases. A constant pressure was maintained during the printing process; however, the ink with higher organic content required higher pressure (4 – 5 bar vs. 2 – 3 bar). The printed samples were dried in the lab at room temperature for 12 h without any precautions.

The rheological properties of the ink were assessed at room temperature using a rotational rheometer (Kinexus Lab+, Netzsch) equipped with a 20 mm plate–plate geometry and a gap of 0.5 mm between the two plates. A special solvent trap assembly was used to minimize the premature drying of the ink. The flow curves were recorded in the shear rate range of 0.1 – 100 s^{-1}. An amplitude sweep test was carried out to determine the linear viscoelastic region (LVR) at a constant frequency of 1 Hz and shear rate range of 0.01 – 100 s^{-1}. The thixotropic response of the ink was measured using a three-interval thixotropy (3iTT) test by subjecting the ink to the following conditions: i) 0.1 % strain for 90 s at 1 Hz; (ii) 200 % strain for 90 s at 1 Hz; (iii) 0.1 % strain for 90 s at 1 Hz.

The dried samples were then simultaneously debinded and sintered in a single-step using different approaches. FF was carried out in a muffle furnace (Nabertherm) preheated to 1550°C. The samples were fastened to a Pt wire and introduced in the furnace chamber through a small hole on the top of the muffle for 5 min before taking them out very quickly.

PSPS was carried out using the DSP-507 sintering press (Dr. Fritsch) with heating/cooling rate of 100 °C/min to 1550 °C and 1600 °C for

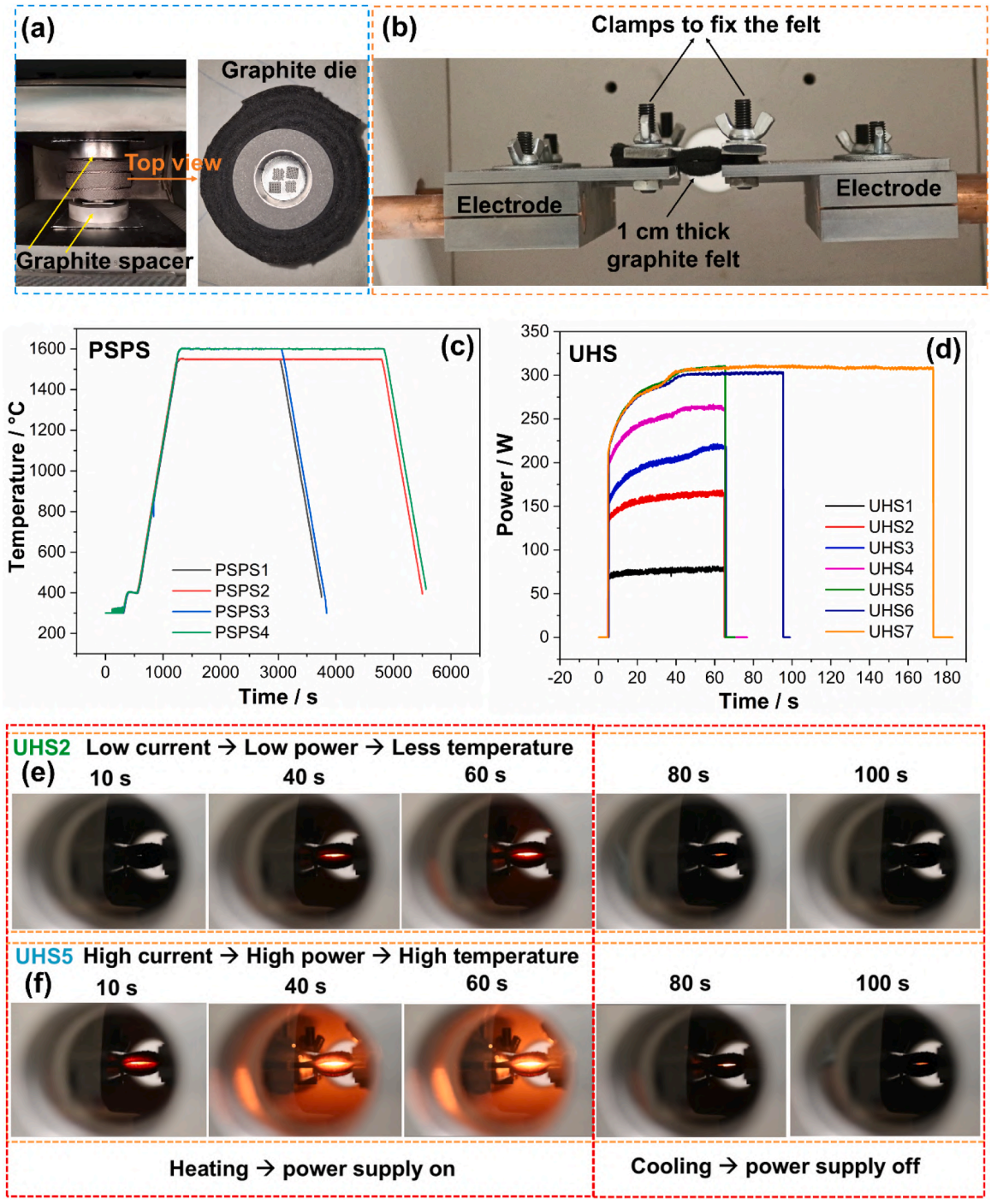

Fig. 1. Optical image of the: (a) Graphite spacer and die used for the PSPS experiments, and (b) UHS setup. The corresponding sintering cycles are shown in (c) and (d), respectively. Snapshots from the real-time UHS experiments with: (e) Lower power, and (f) Higher power, correlating the curves in (d).

different durations (30 min and 60 min at each temperature) as reported in Table 2. A unique circular graphite die assembly (diameter = 30 mm) was employed to transfer the pressure to the die instead of the sample. The graphite die was surrounded by three layers of graphite felt (each approximately 0.5 cm thick) to maintain a homogeneous temperature field inside the graphite die. Fig. 1**(a, c)** shows the used PSPS setup and the heating/cooling profile.

UHS experiments were conducted by placing the sample in a cut made in the center of a 1 cm thick graphite felt (SGL carbon Co., Germany). The felt with a crossection of 24 × 10 mm^2 and length of 24 mm was connected to an AC power supply (TECNA® Item 3484) using steel electrodes, as shown in Fig. 1**(b)**. In this case, electrical power and holding time are the key parameters influencing the sintering process. The UHS setup and the power vs. time diagrams considered here are shown in Fig. 1**(b, d)**. Moreover, the heat evolution in the graphite felt as a function of power has been depicted in Fig. 1**(e-f)**. Higher is the power, higher is the heat generated in the felt and vice versa. The UHS system worked at a fixed AC voltage, but as the graphite felt heats up, it becomes more conductive, which causes the power dissipation to increase over time. This process continues until a steady state is reached (usually in less than 1 min, Fig. 1**(d)**).

UHS and PSPS experiments were carried out in argon atmosphere, while FF was carried out in air. For comparison, conventional sintering (CS) experiments were also carried out in argon with a heating rate of 10

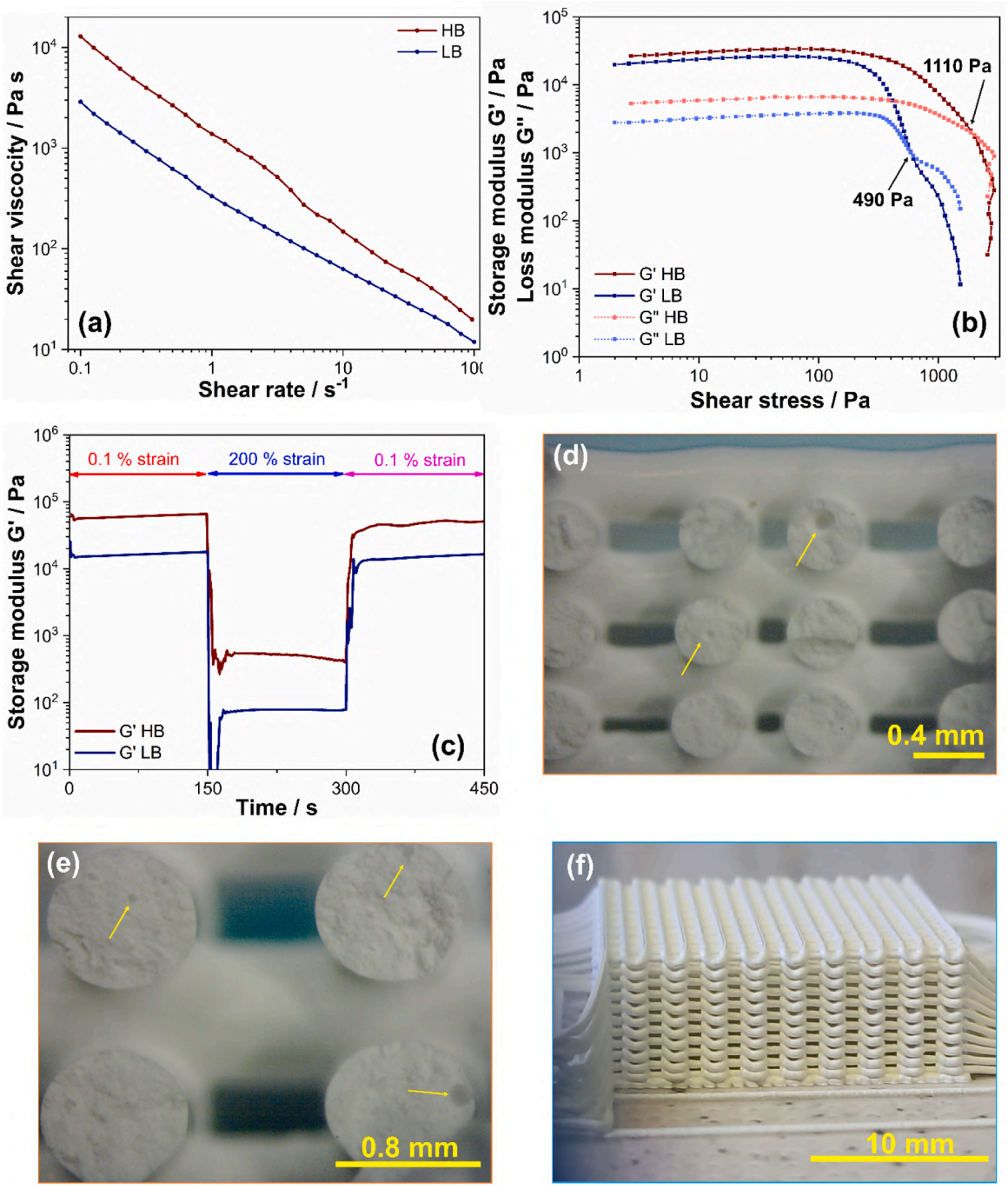

Fig. 2. Rheological data for the prepared inks: (a) Flow curves (b) Amplitude sweep (c) 3iTT. Optical images of the fracture surface of the samples extruded using (d) 0.41 mm and (e) 0.84 mm diameter nozzle. The arrow indicates entrapped bubbles. (f) Optical image of a large size sample showing that the ink is optimized.

°C/min and holding time of 1 h at at varying temperatures ranging from 1400 °C to 1600 °C. The samples were cooled naturally to room temperature. Table 2 summarizes the different sintering conditions used in the present work.

Thermogravimetric analysis (TGA) was performed on fragments from the dried samples in air and argon with a heating rate of 20 °Cmin^{-1} (Netzsch STA 409 thermobalance).

The density of the sintered scaffolds was measured using Archimedes. The phase evolution in the sintered samples was studied by XRD using a θ–2θ diffractometer (Bruker-AXS/D4Endeavor) in the 2θ-range of 20–75° (Δ(2θ) = 0.02° with a scan time of 1 s/step) using Cu Kα radiation (λ = 1.5418 Å). The X-ray source operated at 40 kV and 40 mA.

Raman spectra was recorded on the polished surface with Raman Witec alpha 300 R, using a 532 nm laser with a 50 × objective lens to check the presence of residual carbon in the sintered samples.

The microstructure of the sintered samples was analysed by FE-SEM (TESCAN Solaris, Brno, Czech republic) after sputter-coating with a thin layer of chromium. For the grain size measurements, the samples were polished and thermally etched at 1400 °C for 1 h in argon. At least 100 grains, were measured using ImageJ software [36].

The Vickers microhardness of the sintered samples was measured in 5 different regions on the polished cross-section using a FM-310 microhardness tester with a load of 2 kgf for 15 s.

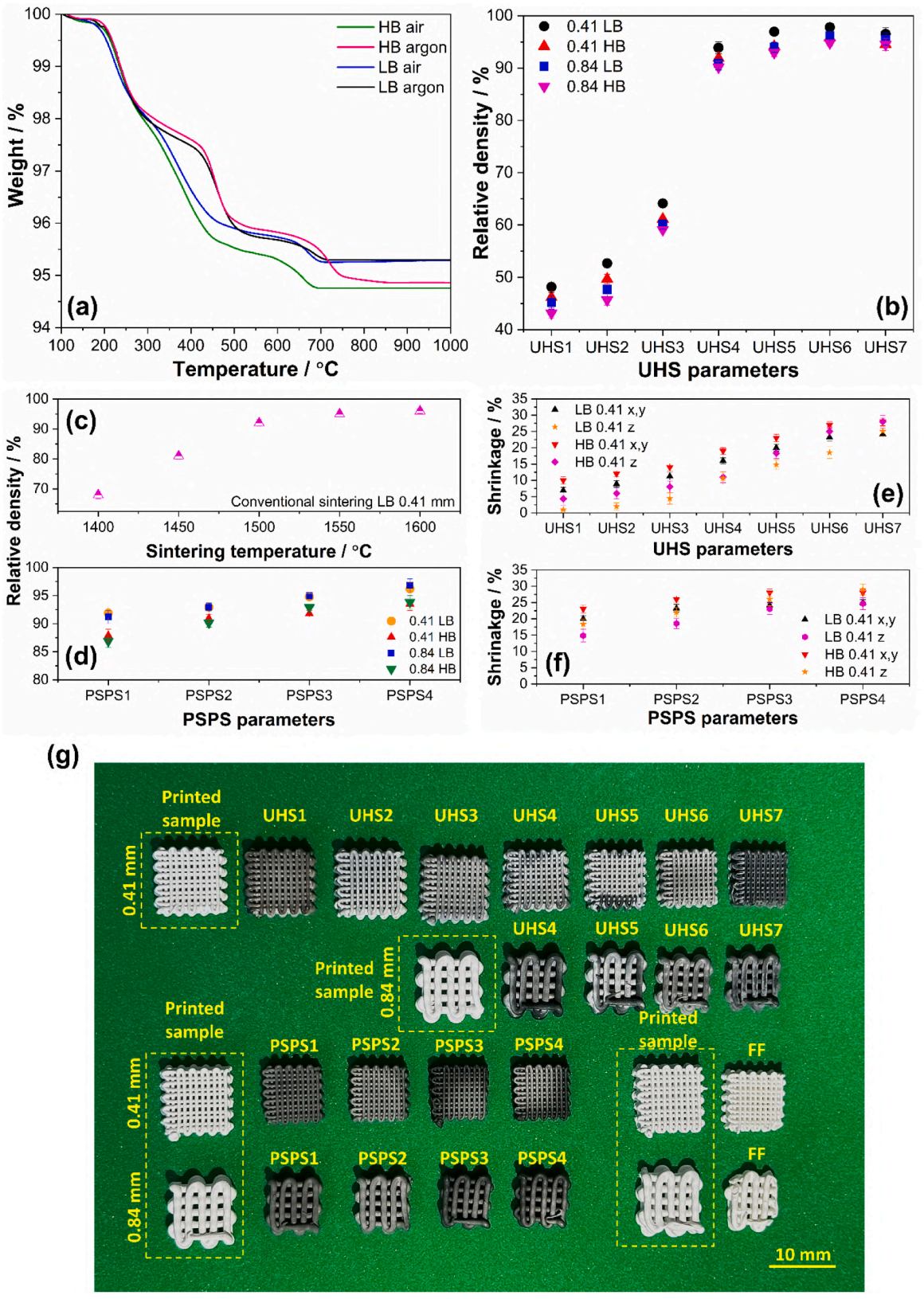

Fig. 3. (a) TGA analysis of the ink in air and argon. (b-f) Variation in density and shrinkage using different sintering processes used. (g) Optical images of the sintered samples. Only the samples fabricated using low organic additives are shown.

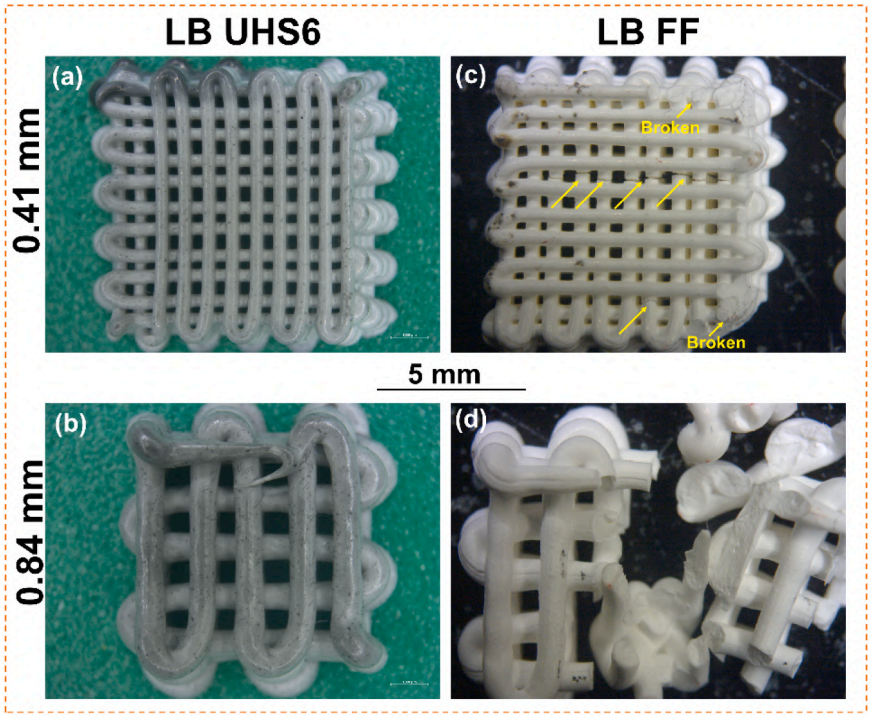

Fig. 4. Optical images of the samples consolidated by: (a-b) UHS, and (c-d) FF.

3. Results and discussion

The rheological properties of the ink play a vital role in dictating the extrusion behaviour and the structural stability of the generated lattice. The flow curves for the prepared ink shown in Fig. 2**(a)** indicate a decrease of viscosity with the applied shear rate, typical of shear-thinning behaviour although a higher viscosity was observed for the ink with larger organic content, very likely correlated with enhanced intermolecular interactions among polymeric chains. Once, the ink is extruded the ability of the extruded struts to sustain their weight is dictated by the storage modulus and the modulus recovery time.

The amplitude sweep test (Fig. 2**(b))** reveals the evolution of the storage and loss modulus as a function of applied shear stress. At low stress values, a linear viscoelastic region can be identified where the storage modulus dominates over the loss modulus. However, as the shear stress increases, G' gradually decreases and at the flow point (τ_f) G'' surpasses G', marking the transition of the ink from solid-like to liquid-like behaviour. The ink with larger organic content shows higher flow point value as reported in Fig. 2**(b)**, indicating greater resistance to flow. This is corroborated by the fact that a higher pressure was required to extrude the ink with larger organic load. The 3-interval thixotropy test (3iTT) reveals a rapid recovery time of ~10 s, where 90 % of the modulus is recovered (Fig. 2**(c))**; this indicates the shape retention ability of the extruded struts. No clear relationship between additives content and recovery time can be observed. The extruded struts with the prepared inks were well optimized with values of $G'_{eq} = 10^3 - 10^5$ Pa (equilibrium storage modulus) and $\tau_f = 490 - 1110$ Pa acceptable for fabricating overhanging structures such as the scaffolds in the present study (Fig. 2**(d-e))** [37]. Such optimized rheological properties ensure smooth and consistent extrusion of the ink, particularly when printing larger structures, as demonstrated in Fig. 2**(f)**. This guarantees uniformity in the printed layers and prevents defects, making it ideal for complex and large-scale applications. Nevertheless, despite these optimizations, some entrapped porosity is observed in the extruded struts, clearly visible and marked with arrows in Fig. 2**(d-e)**.

Fig. 3**(a)** shows the TGA analysis of the dried samples, highlighting that the mass loss occurs predominantly in two different temperature ranges, 250 °C – 450 °C and 450 °C – 750 °C. The initial mass loss observed between 250 °C – 450 °C is associated primarily with the decomposition of PAA, which is completely evolved by around 450 °C [38]. The decomposition of alginate also begins within this range. The subsequent mass loss from 450 °C to 750 °C is predominantly due to the decomposition of alginate [39]. Notably, the mass loss in argon appears to be slightly delayed when compared to air, particularly for the ink with larger amount of binder [40]. However, the overall mass loss seems to be substantially similar, suggesting minor contaminations from the presence of the binder residues when the samples are heated in inert conditions (UHS and PSPS). Furthermore, the residual ceramic content in the formulated inks is in well agreement with the theoretical composition, confirming the homogeneous mixing of the ink.

Unlike vat photopolymerization, where the binder content typically ranges from 20 – 30 wt%, the use of a minimum amount of organic additives in DIW makes it highly suitable for rapid debinding and sintering. This benefit is clearly pointed out by the optical images of the samples processed by UHS and PSPS (Fig. 3**(g))**, where the components retained their shapes without any major defects, this aspect is particularly valuable if one considers that both the debinding and sintering were performed in a few seconds (in UHS) to minutes (in PSPS).

The other critical parameter to be evaluated is the density of the sintered sample. Fig. 3**(b-d)** shows the evolution of density as a function of UHS, PSPS, and CS parameters. One can clearly observe that the density increases with UHS power and holding time, reaching a maximum of ~97 %. The conventional sintering samples exhibit a similar trend, with densities improving as the sintering temperature increases. With a prolonged holding time of 180 s at the highest UHS power (UHS7), a slight decrease in the density is observed probably associated to the carbothermal decomposition of alumina at very high temperature (this argument will be further supported by the microstructure discussed in the following sections). Also, in PSPS the relative density increases with firing time and temperature.

It is worth noting that the density obtained by PSPS (≈96 %) and UHS (≈98 %) is larger than that achievable by conventional sintering at 1500°C for 1 h (≈95 %), thus corroborating the idea that rapid heating can boost densification. Therefore, rapid sintering of DIW alumina does

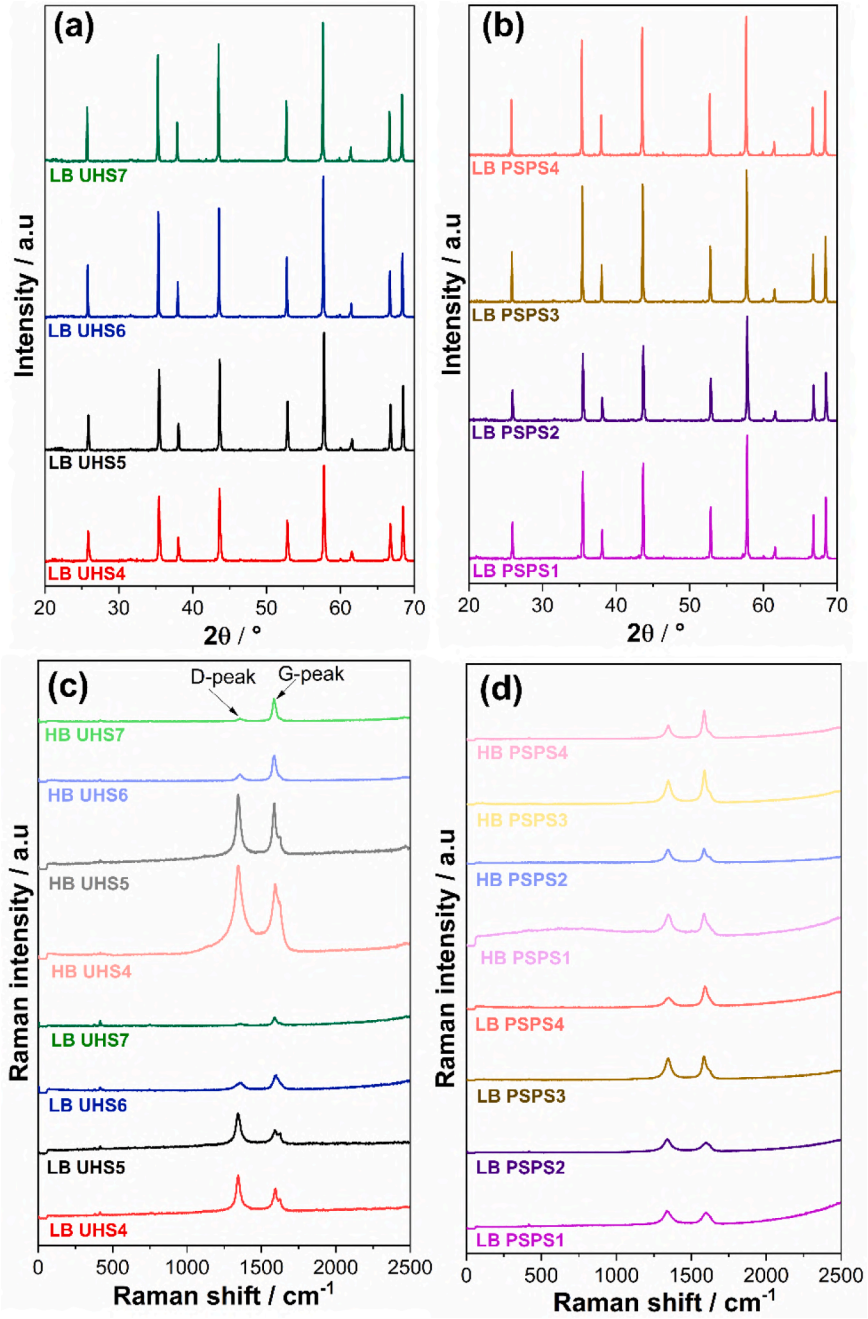

Fig. 5. XRD spectra of LB samples processed by: (a) UHS, and (b) PSPS. Raman spectra of LB and HB samples consolidated using: (c) UHS, and (d) PSPS. This analysis was carried out on the samples fabricated with 0.41 mm nozzle diameter.

not only allow to reduce the sintering time but provides also a detectable improvement in density.

The density is also influenced by the ink composition and the strut thickness as shown in Fig. 3**(b, d)**. In particular, a larger amount of binder (and solvent) in the ink causes a small but detectable reduction in the final density of the bodies processed by both PSPS and UHS; conversely, the shrinkage is greater when considering the HB composition (Fig. 3**(e-f)**). The results can be rationalized by considering that the LB ink allows to obtain green bodies with higher density after printing.

On the other hand, the samples printed with the 0.84 mm nozzle are systematically less dense. An accurate measurement of the sintering shrinkage was not possible for the material printed with wider nozzle since the geometry is not regular enough. One could suggest that during rapid heating the temperature distribution in the case of thick struts can be inhomogeneous thus reducing the final density; nevertheless, no microstructural evidence of substantial thermal gradients were recorded by SEM. The most likely cause of the nozzle size-dependent density in the sintered materials is a variation in the green body density.

The evolution of the sintering shrinkage with firing conditions is in well agreement with the density measurements (Fig. 3**(e-f)**). In general, due to the layer-by-layer fabrication process, the shrinkage along the Z direction is expected to be higher than in the x/y direction. However, in our case, the opposite trend was observed. This can be due to the excellent interlayer bonding as shown from the fracture surfaces of the printed sample in Fig. 2**(d-e)** [41].

Interestingly, the results are substantially different when rapid sintering is carried out in air. In fact, the fast-fired samples appear fractured irrespectively of the strut thickness (Fig. 4**(c-d)**). Although the samples

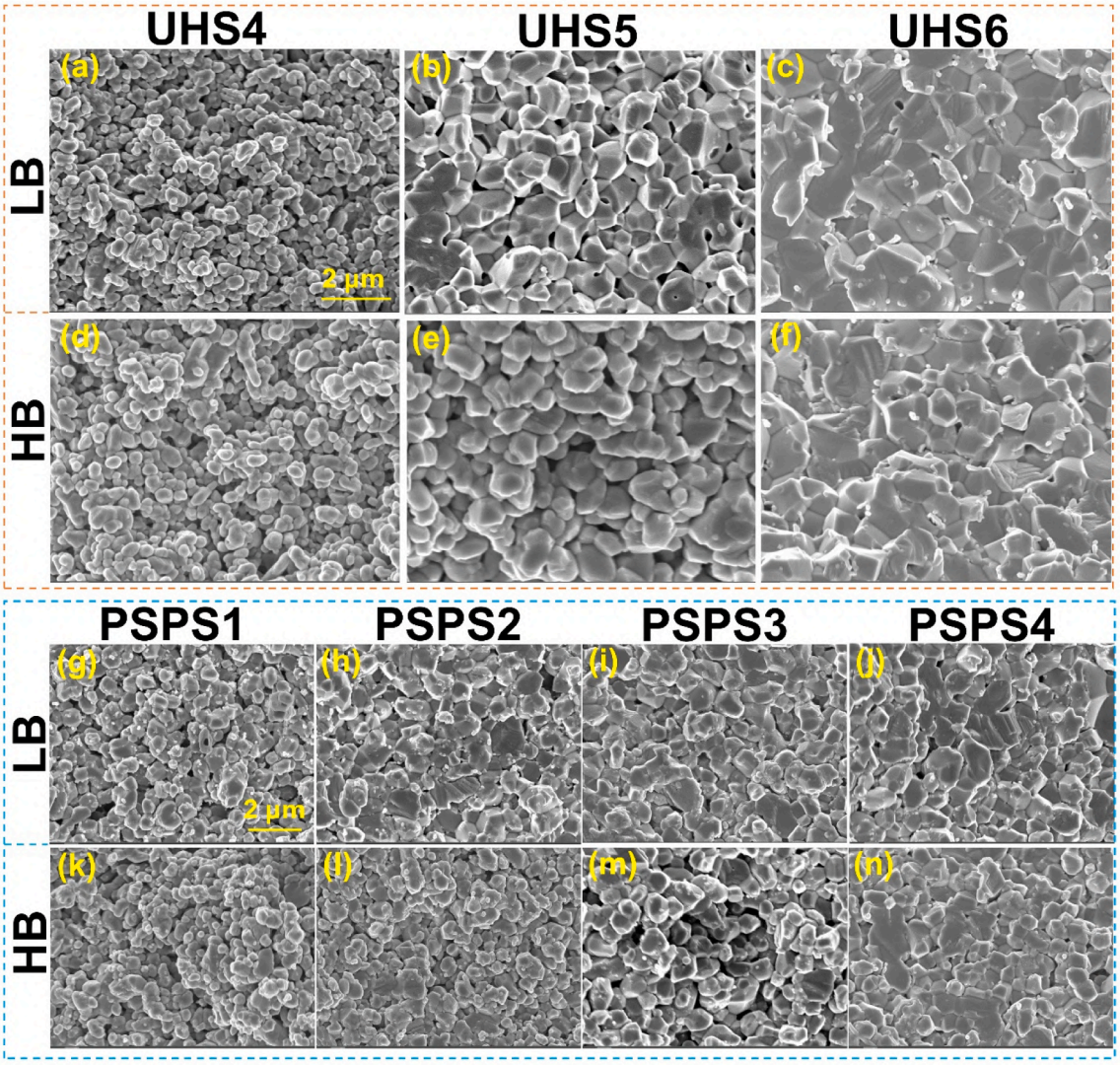

Fig. 6. SEM images of the fracture surface of LB and HB samples fabricated with 0.41 mm nozzle diameter and processed using: (a-f) UHS, and (g-n) PSPS.

retained their overall shape, the severity of the cracks was significant, causing them to shatter when using the 0.84 mm nozzle diameter. The sintering atmosphere plays a crucial role in determining the organics decomposition [42,43]. In air, additives undergo exothermic decomposition in the presence of oxygen leading to violent reactions. Conversely, the decomposition in argon occurs by endothermic thermolysis which requires longer times to be completed. This violent decomposition in air is likely to produce internal stress leading to cracks in the sample as shown in Fig. 4**(c-d)**.

The fracture surfaces microstructure on the cracks formed during FF is characterized by curved grain surfaces, with no sharp edges or faceted geometries (Fig. S1(a)). This suggests that the cracks were produced during the heating phase, likely as a result of thermal stress due to the binder combustion. In contrast, fracture surfaces created manually for comparison exhibit faceted grains **(**Fig. S1**(b))**.

The mineralogical analysis carried out by XRD reveals the presence of pure α-Al_2O_3 according to JCPDS: 00–005–0712, without any secondary phases **(**Fig. 5**(a-b))**. One can observe from Fig. 3**(f)** that the samples after UHS or PSPS exhibit grey or dark coloration, which can be related to the reduction of the oxide or the presence of carbon [44,45]. In order to check the evolution of the carbon in the sintered samples, Raman analysis was carried out and the recorded spectra are shown in Fig. 5**(c-d)**. The presence of residual carbon is revealed in all sintered samples with a noticeable difference in the intensity ratio of the D and G peaks, which decreases with UHS power or PSPS temperature. This variation in the peak's intensity suggests a change in the order of the residual carbon. At lower currents or temperatures, the high I_D/I_G ratio indicates the presence of a disordered or amorphous carbon generated by the pyrolysis of the organic additives. By increasing UHS power or PSPS temperature, the I_D/I_G ratio decreases, suggesting a transition from disordered to ordered carbon phase [46], this latter is very likely deposited from the graphite felt or die at higher temperature. Similar observations are also reported in a previous work describing the SPS of $MgAl_2O_4$ [47]. In addition, D and G peaks appear more intense in the HB samples, likely due to the higher amount of residual carbon, as pointed out by the TGA analysis in Fig. 2**(a)**.

Fig. 6 shows the fracture surface of the sintered samples. By increasing the UHS power or PSPS temperature, the density increases, this is in consistent with the results shown in Fig. 3**(b, d)**. A transition from intergranular to transgranular fracture can also be observed by increasing UHS power or PSPS temperature. Such transformation of fracture mechanism for alumina is well-established [45].

The observation of the external surface of the sample UHS7 shed light on the origin of the small density reduction when UHS is carried out at the highest power as shown in Fig. 3**(b)**. At high temperature, carbothermal reduction of alumina occurs, forming $AlO_{(g)}$, $CO_{(g)}$, and $Al_4C_{3\,(s)}$ [48–50]. Al_4C_3 further reacts with Al_2O_3 to produce Al and CO, aluminium vaporizing and leaving behind a porous structure. The

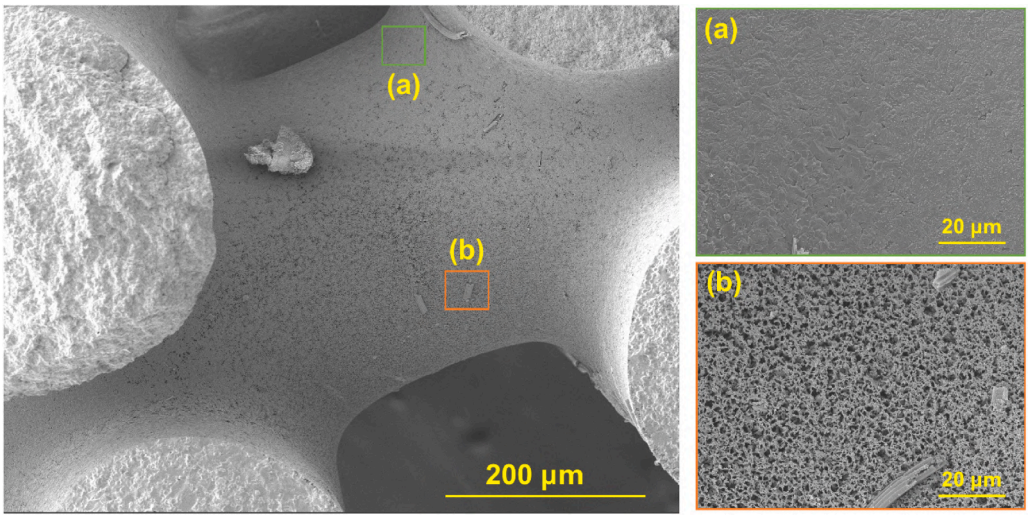

Fig. 7. SEM image showing the external surface of the sample processed by UHS with the highest power (UHS7). Position (b) is close to the graphite felt, while position (a) corresponds to the core of the sample.

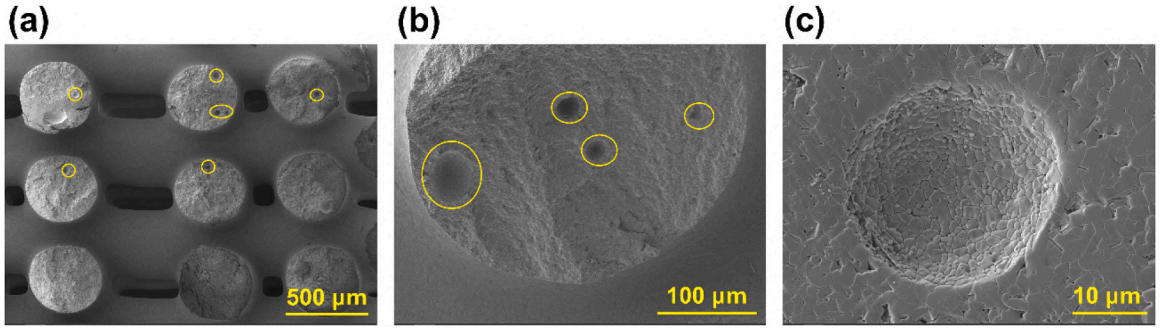

Fig. 8. (a-b) Overview, and (b) Magnified SEM images of the entrapped bubble in the printed sample (marked in yellow circles). (c) Magnified SEM image of the entrapped pore in the sintered sample.

formation of porosity at the sample surface is confirmed in Fig. 7. Specifically, only the regions of the sample in physical contact with the felt show such porous features **(**Fig. 7**(b))**, the inner surfaces of the lattice remaining instead dense **(**Fig. 7**(a))**. It is, therefore, possible to infer that the porosity originates from the reaction between the sample and the felt.

The achievement of full densification in additively manufactured ceramics still remains a challenge. One of the most significant factors affecting density is the entrapment of air bubbles (see Fig. 2**(d-e)** and Fig. 8), especially for inks with higher ceramic loadings. Such large pores are characterized by low capillarity stresses and long diffusion distances that cannot be eliminated during firing. One can, therefore, emphasize that the rapid sintering process analysed in the present work was fully successful in densifying the component, while further optimizations of the ink composition and printing procedure are still possible.

Fig. 9 shows the microstructure of the sintered samples after polishing and thermal etching. By increasing the UHS power or PSPS temperature/hold time, density and grain size increases. Some residual porosity is quite evident in the samples that were fabricated with higher organic load **(**Fig. 9**(d-f, g-j))**, thus confirming the density data in Fig. 3 **(b-c)**.

Furthermore, one can also observe that UHS and PSPS allow for a fine microstructure while maintaining high density **(**Fig. 9**(m))**. For instance, specimens processed under UHS4 **(**Fig. 9**(a))**, UHS5 **(**Fig. 9**(b))**, PSPS3 **(**Fig. 9**(g))** conditions, exhibit better or almost the same densification as the conventionally sintered one **(**Fig. 9**(k-l))**, while retaining the fine microstructure. One might suggest that the atmosphere impacts the observed grain refinement. While an atmosphere effect cannot be excluded, it can be emphasized that the grain size *vs*. density trajectory in UHS still remains beneath the PSPS one, thus pointing out that also the heating rate has a substantial impact. This confirms that rapid heating in UHS (and, to a lower extent, in PSPS) has a beneficial effect on densification and microstructural evolution, in agreement with other ceramics systems [9,14].

The hardness of the samples as a function of the relative density is reported in Fig. 9**(n)**. Samples UHS4 and PSPS3 exhibited low hardness values due to their lower density. In contrast, as density increased while retaining a fine microstructure, sample UHS5 demonstrated hardness values comparable to or even exceeding those of conventionally sintered samples at 1600 °C. However, further increases in density led to grain growth and a slight decrease in hardness, as observed in sample UHS6.

Interestingly, sample PSPS4 showed lower hardness despite its finer microstructure compared to a similarly dense sample processed conventionally. This discrepancy might be attributed to the presence of residual carbon, as evidenced by significantly higher carbon peak intensities in PSPS4 compared to the UHS samples, indicating greater residual carbon content.

4. Conclusions

In this study, optimized alumina inks with suitable rheology for DIW process was used to produced log-pile structures, designed specifically for rapid debinding and densification. Rapid sintering was successfully

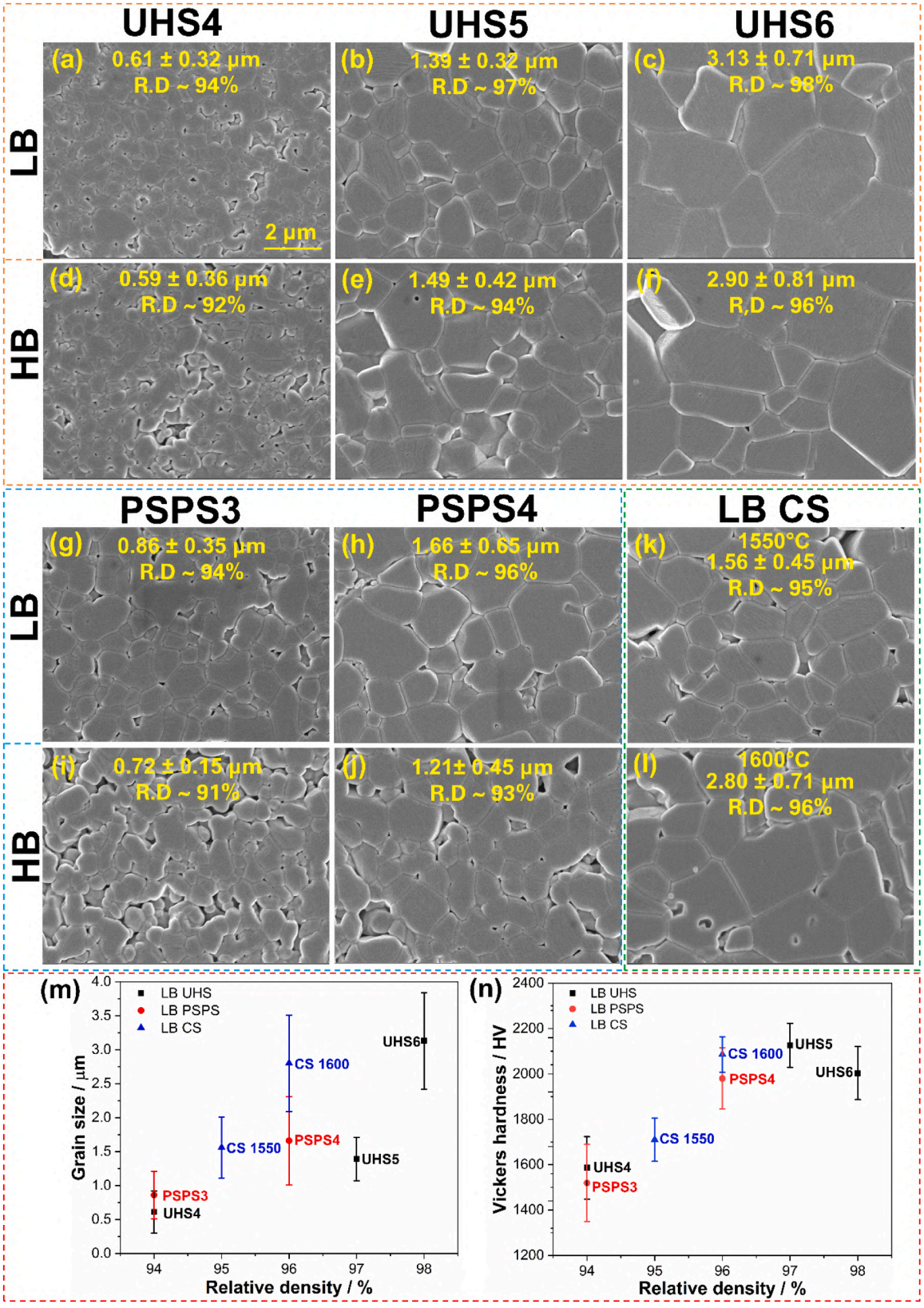

Fig. 9. SEM images of the polished/etched cross-section for LB and HB samples fabricated with 0.41 mm nozzle diameter and consolidated by: (a-f) UHS, and (g-j) PSPS. (k-l) Microstructure of the LB samples conventionally sintered at different temperatures for 1 h. Evolution of the: (m) Grain size, and (n) Hardness as a function of the relative density for LB samples.

accomplished by UHS and PSPS in Ar, while cracks were observed in the samples fast-fired in air. It is worth emphasizing that both debinding and sintering were carried out in a single step (i.e., without the need of additional debinding cycle).

The ceramic loading in the ink and the printing nozzle size significantly influence the densification process and larger binder content (lower ceramic loading) and wider nozzle size (0.84 mm vs. 0.41 mm) led to reduced density after sintering. PSPS and UHS allow for well-sintered alumina artifacts in seconds/minutes with a density exceeding that achievable by conventional heating (1550 °C for 1 h). Interestingly, UHS (and PSPS to a lower extent) promotes consolidation with reduced grain coarsening, the grain size scaling inversely with the heating rate.

This approach of debinding and sintering can be applied to various compositions and shapes, enabling energy-efficient processing of ceramics.

CRediT authorship contribution statement

Giorgia Franchin: Writing – review & editing, Supervision, Resources, Project administration, Methodology, Conceptualization. **Vincenzo M. Sglavo:** Writing – review & editing, Supervision, Resources. **Mattia Biesuz:** Writing – review & editing, Supervision, Resources, Methodology, Conceptualization. **Milad Kermani:** Writing – review & editing, Investigation, Data curation. **Subhadip Bhandari:** Writing – original draft, Validation, Methodology, Investigation, Funding acquisition, Formal analysis, Data curation, Conceptualization. **Ondrej Hanzel:** Writing – review & editing, Investigation, Funding acquisition.

Declaration of Competing Interest

The authors declare the following financial interests/personal relationships which may be considered as potential competing interests: Subhadip Bhandari reports was provided by Foundation of the Savings Bank of Padua and Rovigo. Vincenzo M. Sglavo reports financial support was provided by Ministero delle Imprese e del Made in Italy. Ondrej Hanzel reports financial support was provided by Slovak Grant Agency VEGA and Slovak Research and Development Agency. If there are other authors, they declare that they have no known competing financial interests or personal relationships that could have appeared to influence the work reported in this paper.

Acknowledgements

Subhadip Bhandari gratefully acknowledges the CARIPARO Foundation for the PhD scholarship. Dr. Lisa Santello is acknowledged for the Raman analysis. The Ministero delle Imprese e del Made in Italy is acknowledged by VMS for the financial support under the project PRINCE, Prog. n. F/310085/02/X56 - CUP: B69J23000210005 – COR: 10609513. This work was also financially supported by the Slovak Grant Agency VEGA Project No. 2/0007/21 and Slovak Research and Development Agency, Contract No.APVV-21-0402.

Appendix A. Supporting information

Supplementary data associated with this article can be found in the online version at doi:10.1016/j.jeurceramsoc.2024.117144.

References

[1] ISO/ASTM 52900:2021(en), Additive manufacturing — General principles — Fundamentals and vocabulary, (n.d.). ⟨https://www.iso.org/obp/ui/#iso:std:iso-astm:52900:ed-2:v1:en⟩ (accessed December 20, 2023).
[2] S. Lamnini, H. Elsayed, Y. Lakhdar, F. Baino, F. Smeacetto, E. Bernardo, Robocasting of advanced ceramics: ink optimization and protocol to predict the printing parameters - a review, Heliyon 8 (2022), https://doi.org/10.1016/J.HELIYON.2022.E10651.
[3] E. Peng, D. Zhang, J. Ding, E. Peng, D. Zhang, J. Ding, Ceramic robocasting: recent achievements, potential, and future developments, Adv. Mater. 30 (2018) 1802404, https://doi.org/10.1002/ADMA.201802404.
[4] M.A.S.R. Saadi, A. Maguire, N.T. Pottackal, M.S.H. Thakur, M.M. Ikram, A.J. Hart, P.M. Ajayan, M.M. Rahman, Direct ink writing: a 3D printing technology for diverse materials, Adv. Mater. 34 (2022) 2108855, https://doi.org/10.1002/ADMA.202108855.
[5] L. del-Mazo-Barbara, M.P. Ginebra, Rheological characterisation of ceramic inks for 3D direct ink writing: a review, J. Eur. Ceram. Soc. 41 (2021) 18–33, https://doi.org/10.1016/J.JEURCERAMSOC.2021.08.031.
[6] R.L. Walton, M.J. Brova, B.H. Watson, E.R. Kupp, M.A. Fanton, R.J. Meyer, G. L. Messing, Direct writing of textured ceramics using anisotropic nozzles, J. Eur. Ceram. Soc. 41 (2021) 1945–1953, https://doi.org/10.1016/j.jeurceramsoc.2020.10.021.
[7] H.J. Chen, P.Y. Lee, C.Y. Chen, S.L. Huang, B.W. Huang, F.J. Dai, C.F. Chau, C. S. Chen, Y.S. Lin, Moisture retention of glycerin solutions with various concentrations: a comparative study, Sci. Rep. 12 (2022), https://doi.org/10.1038/S41598-022-13452-2.
[8] Z. Lotfizarei, A. Mostafapour, A. Barari, A. Jalili, A.E. Patterson, Overview of debinding methods for parts manufactured using powder material extrusion, Addit. Manuf. 61 (2023) 103335, https://doi.org/10.1016/J.ADDMA.2022.103335.
[9] M. Kermani, C. Hu, S. Grasso, From pit fire to Ultrafast High-temperature Sintering (UHS): a review on ultrarapid consolidation, Ceram. Int. 49 (2023) 4017–4029, https://doi.org/10.1016/J.CERAMINT.2022.11.091.
[10] M. Biesuz, S. Grasso, V.M. Sglavo, What's new in ceramics sintering? A short report on the latest trends and future prospects, Curr. Opin. Solid State Mater. Sci. 24 (2020) 100868, https://doi.org/10.1016/j.cossms.2020.100868.
[11] S. Bhandari, O. Hanzel, P. Veteška, M. Janek, E. De Bona, V.M. Sglavo, M. Biesuz, G. Franchin, From rapid prototyping to rapid firing: on the feasibility of high-speed production for complex BaTiO3 components, J. Am. Ceram. Soc. (2024), https://doi.org/10.1111/JACE.19950.
[12] S. Bhandari, C. Manière, F. Sedona, E. De Bona, V.M. Sglavo, P. Colombo, L. Fambri, M. Biesuz, G. Franchin, Ultra-rapid debinding and sintering of additively manufactured ceramics by ultrafast high-temperature sintering, J. Eur. Ceram. Soc. 44 (2024) 328–340, https://doi.org/10.1016/J.JEURCERAMSOC.2023.08.040.
[13] M.N. Rahaman, Ceramic processing and sintering, second edition, Ceram. Process. Sinter., Second Ed. (2017) 1–875, https://doi.org/10.1201/9781315274126/CERAMIC-PROCESSING-SINTERING-MOHAMED-RAHAMAN.
[14] M H.A.R.M.E.R., B R.J., Fast firing - microstructural benefits, fast firing - microstructural benefits (1981).
[15] D.E. García, J. Seidel, R. Janssen, N. Claussen, Fast firing of alumina, J. Eur. Ceram. Soc. 15 (1995) 935–938, https://doi.org/10.1016/0955-2219(95)00071-2.
[16] M. Biesuz, L. Spiridigliozzi, M. Frasnelli, G. Dell'Agli, V.M. Sglavo, Rapid densification of Samarium-doped Ceria ceramic with nanometric grain size at 900–1100 °C, Mater. Lett. 190 (2017) 17–19, https://doi.org/10.1016/J.MATLET.2016.12.132.
[17] K.K. Singh, Subrahmanyam, Fast firing of ceramics—a review, Trans. Indian Ceram. Soc. 35 (1976) 26–30, https://doi.org/10.1080/0371750X.1976.10840848.
[18] R. Yamanoglu, Pressureless spark plasma sintering: a perspective from conventional sintering to accelerated sintering without pressure, Powder Metall. Met. Ceram. 2019 57:9 57 (2019) 513–525, https://doi.org/10.1007/S11106-019-00010-1.
[19] C. Wang, W. Ping, Q. Bai, H. Cui, R. Hensleigh, R. Wang, A.H. Brozena, Z. Xu, J. Dai, Y. Pei, C. Zheng, G. Pastel, J. Gao, X. Wang, H. Wang, J.-C. Zhao, B. Yang, X. (Rayne) Zheng, J. Luo, Y. Mo, B. Dunn, L. Hu, A general method to synthesize and sinter bulk ceramics in seconds, Science 368 (2020) 521–526, https://doi.org/10.1126/science.aaz7681.
[20] E. De Bona, L. Karacasulu, C. Vakifahmetoglu, V.M. Sglavo, M. Biesuz, Ultrafast high-temperature sintering (UHS) of WC and WC-containing ZrB2, J. Alloy. Compd. 986 (2024), https://doi.org/10.1016/J.JALLCOM.2024.174102.
[21] E. De Bona, C. Manière, V.M. Sglavo, M. Biesuz, Ultrafast high-temperature sintering (UHS) of ZrB2-based materials, J. Eur. Ceram. Soc. (2023), https://doi.org/10.1016/J.JEURCERAMSOC.2023.09.007.
[22] R.F. Guo, H.R. Mao, Z.T. Zhao, P. Shen, Ultrafast high-temperature sintering of bulk oxides, Scr. Mater. 193 (2021) 103–107, https://doi.org/10.1016/J.SCRIPTAMAT.2020.10.045.
[23] M. Kermani, D. Zhu, J. Li, J. Wu, Y. Lin, Z. Dai, C. Hu, S. Grasso, Ultra-fast High-temperature Sintering (UHS) of translucent alumina, Open Ceram. 9 (2022) 100202, https://doi.org/10.1016/J.OCERAM.2021.100202.
[24] J. Wu, Y. Lin, C. Hu, S. Grasso, D. Zhu, J. Li, A. Katz-Demyanitcz, A. Goldstein, Ultra-fast high-temperature sintering of transparent MgAl2O4, Ceram. Int. 49 (2023) 19537–19540, https://doi.org/10.1016/J.CERAMINT.2023.03.018.
[25] L. Spiridigliozzi, G. Dell'Agli, S. Esposito, P. Rivolo, S. Grasso, V.M. Sglavo, M. Biesuz, Ultra-fast high-temperature sintering (UHS) of Ce0.2Zr0.2Y0.2Gd0.2La0.2O2−δ fluorite-structured entropy-stabilized oxide (F-ESO), Scr. Mater. 214 (2022) 114655, https://doi.org/10.1016/J.SCRIPTAMAT.2022.114655.
[26] R.-X. Luo, M. Kermani, Z.-L. Guo, J. Dong, C.-F. Hu, F. Zuo, S. Grasso, B.-B. Jiang, G.-L. Nie, Z.-Q. Yan, Q. Wang, Y.-L. Gan, F.-P. He, H.-T. Lin, Ultrafast high-temperature sintering of silicon nitride: a comparison with the state-of-the-art techniques, J. Eur. Ceram. Soc. 41 (2021) 6338–6345, https://doi.org/10.1016/j.jeurceramsoc.2021.06.021.
[27] M. Biesuz, A. Galotta, A. Motta, M. Kermani, S. Grasso, J. Vontorová, V. Tyrpekl, M. Vilémová, V.M. Sglavo, Speedy bioceramics: rapid densification of tricalcium

phosphate by ultrafast high-temperature sintering, Mater. Sci. Eng. C 127 (2021) 112246, https://doi.org/10.1016/j.msec.2021.112246.
[28] M. Ihrig, T.P. Mishra, W.S. Scheld, G. Häuschen, W. Rheinheimer, M. Bram, M. Finsterbusch, O. Guillon, Li7La3Zr2O12 solid electrolyte sintered by the ultrafast high-temperature method, J. Eur. Ceram. Soc. 41 (2021) 6075–6079, https://doi.org/10.1016/j.jeurceramsoc.2021.05.041.
[29] J. Dong, V. Pouchly, M. Biesuz, V. Tyrpekl, M. Vilémová, M. Kermani, M. Reece, C. Hu, S. Grasso, Thermally-insulated ultra-fast high temperature sintering (UHS) of zirconia: a master sintering curve analysis, Scr. Mater. 203 (2021) 114076, https://doi.org/10.1016/J.SCRIPTAMAT.2021.114076.
[30] M. Kermani, J. Dong, M. Biesuz, Y. Linx, H. Deng, V.M. Sglavo, M.J. Reece, C. Hu, S. Grasso, Ultrafast high-temperature sintering (UHS) of fine grained α-Al2O3, J. Eur. Ceram. Soc. 41 (2021) 6626–6633, https://doi.org/10.1016/J.JEURCERAMSOC.2021.05.056.
[31] M.J.H. Reavley, H. Guo, J. Yuan, A.Y.R. Ng, T.Y.K. Ho, H.T. Tan, Z. Du, C.L. Gan, Ultrafast high-temperature sintering of barium titanate ceramics with colossal dielectric constants, J. Eur. Ceram. Soc. 42 (2022) 4934–4943, https://doi.org/10.1016/J.JEURCERAMSOC.2022.04.056.
[32] C. Paredes, J. Roleček, L. Pejchalová, T. Spusta, D. Salamon, P. Miranda, Evaluating the suitability of fast sintering techniques for the consolidation of calcium phosphate scaffolds produced by DLP, J. Eur. Ceram. Soc. 43 (2023) 6493–6503, https://doi.org/10.1016/J.JEURCERAMSOC.2023.05.052.
[33] A.K. Hofer, A. Kocjan, R. Bermejo, High-strength lithography-based additive manufacturing of ceramic components with rapid sintering, Addit. Manuf. 59 (2022) 103141, https://doi.org/10.1016/J.ADDMA.2022.103141.
[34] S. Eqtesadi, A. Motealleh, F.H. Perera, P. Miranda, A. Pajares, R. Wendelbo, F. Guiberteau, A.L. Ortiz, Fabricating geometrically-complex B4C ceramic components by robocasting and pressureless spark plasma sintering, Scr. Mater. 145 (2018) 14–18, https://doi.org/10.1016/j.scriptamat.2017.10.001.
[35] I. Barisic, R. Brucculeri, L. Airoldi, Z. Warren, A.S. Martins, M. Coduri, F. Auricchio, U.T. Anselmi, D. Mattia, Fast sintering of titania monoliths for photocatalytic degradation of organic micropollutants, Appl. Mater. Today 38 (2024) 102172, https://doi.org/10.1016/J.APMT.2024.102172.
[36] C.A. Schneider, W.S. Rasband, K.W. Eliceiri, NIH Image to ImageJ: 25 years of image analysis, Nat. Methods 2012 9:7 9 (2012) 671–675, https://doi.org/10.1038/nmeth.2089.
[37] L. del-Mazo-Barbara, M.P. Ginebra, Rheological characterisation of ceramic inks for 3D direct ink writing: A review, J. Eur. Ceram. Soc. 41 (2021) 18–33, https://doi.org/10.1016/J.JEURCERAMSOC.2021.08.031.
[38] V. Datsyuk, L. Billon, C. Guerret-Piécourt, S. Dagréou, N. Passade-Boupatt, S. Bourrigaud, O. Guerret, L. Couvreur, In situ nitroxide-mediated polymerized poly(acrylic acid) as a stabilizer/compatibilizer carbon nanotube/polymer composites, J. Nanomater. 2007 (2007), https://doi.org/10.1155/2007/74769.
[39] A.F. Hassan, H.M.A. salam, F. Mohamed, O.F. Abdel-Gawad, The optimization performance of fibrous sodium alginate co-polymer in direct methanol/ethanol fuel cells, J. Polym. Environ. 31 (2023) 3664–3676, https://doi.org/10.1007/S10924-023-02852-8/FIGURES/7.
[40] E. Esmizadeh, C. Tzoganakis, T.H. Mekonnen, Degradation behavior of polypropylene during reprocessing and its biocomposites: thermal and oxidative degradation kinetics, Polymers 12 (2020), https://doi.org/10.3390/POLYM12081627.
[41] S. Bhandari, P. Veteška, G. Vajpayee, M. Hinterstein, Z. Bača, Z. Hajdúchová, G. Špitalský, M. Franchin, Janek, Material-extrusion based additive manufacturing of BaTiO3 ceramics: from filament production to sintered properties, Addit. Manuf. 88 (2024) 104238, https://doi.org/10.1016/J.ADDMA.2024.104238.
[42] S. Zhou, G. Liu, C. Wang, Y. Zhang, C. Yan, Y. Shi, Thermal debinding for stereolithography additive manufacturing of advanced ceramic parts: a comprehensive review, Mater. Des. 238 (2024) 112632, https://doi.org/10.1016/J.MATDES.2024.112632.
[43] H. Li, Y. Liu, Y. Liu, K. Hu, Z. Lu, J. Liang, Investigating the relation between debinding atmosphere and mechanical properties of stereolithography-based three-dimensional printed Al2O3 ceramic, Proc. Inst. Mech. Eng. Part B J. Eng. Manuf. 234 (2020) 1686–1694, https://doi.org/10.1177/0954405420937855.
[44] A. Kabir, B. Lemieszek, J. Karczewski, E. De Bona, M. Varenik, S. Molin, M. Biesuz, Ultrafast high-temperature sintering (UHS) of cerium oxide-based compound, Open Ceram. 17 (2024) 100551, https://doi.org/10.1016/J.OCERAM.2024.100551.
[45] R. Marder, P. Ghosh, I. Reimanis, W.D. Kaplan, The influence of carbon on the microstructure and wear resistance of alumina, J. Am. Ceram. Soc. 104 (2021) 4214–4225, https://doi.org/10.1111/JACE.17832.
[46] A. Ferrari, J. Robertson, Interpretation of Raman spectra of disordered and amorphous carbon, Phys. Rev. B 61 (2000) 14095, https://doi.org/10.1103/PhysRevB.61.14095.
[47] K. Morita, B.N. Kim, H. Yoshida, K. Hiraga, Y. Sakka, Distribution of carbon contamination in MgAl2O4 spinel occurring during spark-plasma-sintering (SPS) processing: I – effect of heating rate and post-annealing, J. Eur. Ceram. Soc. 38 (2018) 2588–2595, https://doi.org/10.1016/J.JEURCERAMSOC.2017.09.038.
[48] Y.K. Folomeikin, I.M. Demonis, E.N. Kablov, S.I. Lopatin, V.L. Stolyarova, Investigation into the vaporization of Al2O3 in the presence of carbon at high temperatures, Glass Phys. Chem. 32 (2006) 191–195, https://doi.org/10.1134/S1087659606020118.
[49] S.K. Mishra, S.K. Das, L.C. Pathak, Sintering behaviour of self-propagating high temperature synthesised ZrB2-Al2O3 composite powder, Mater. Sci. Eng.: A 426 (2006) 229–234, https://doi.org/10.1016/j.msea.2006.04.026.
[50] P. Lefort, M. Billy, Mechanism of AlN formation through the carbothermal reduction of Al2O3 in a flowing N2 atmosphere, J. Am. Ceram. Soc. 76 (1993) 2295–2299, https://doi.org/10.1111/J.1151-2916.1993.TB07767.X.